Supporting Information for "Ductile Copper Hydride Eliashberg Superconductors with T_c in Liquid-Nitrogen Temperature Range and Band Topology at Ambient Pressure"

Chong Tian,[1] Yao-hui Zhu,[2,*] Juan Du,[3] Hong-xia Zhong,[4] Jing Lu,[1] Xinqiang Wang,[1] and Jun-jie Shi[1,†]
[1]*State Key Laboratory for Artificial Microstructures and Mesoscopic Physics, School of Physics,*
Peking University Yangtze Delta Institute of Optoelectronics, Peking University, Beijing 100871, China
[2]*Physics Department, Beijing Technology and Business University, Beijing 100048, China*
[3]*Department of Physics and Optoelectronic Engineering Faculty of Science,*
Beijing University of Technology, Beijing 100124, China and
[4]*School of Mathematics and Physics, China University of Geosciences, Wuhan 430074, China*
(Dated: March 20, 2025)

I. COMPUTATIONAL DETAILS

A. Impact of the On-Site Coulomb Interactions on Structure, Electron and Phonon Properties

Generally, generalized gradient approximation (GGA) functionals within the single-particle approximation provide satisfactory results for the crystal structure, band structure, and superconducting properties of most systems. However, for systems including localized d and f orbitals, particularly transition metal oxides or nitrides, deviations arise owing to the strong correlation effect of electron. In Cu_4H_3, a part of the Cu 3d orbitals lies near the Fermi level (E_F). Therefore, we account for the on-site Coulomb interactions and investigate their impact on the structure and electron properties of Cu_4H_3 using the GGA+U method implanted in the Quantum ESPRESSO package. To determine the Hubbard U value for Cu, we note that the linear response method is unsuitable for the closed-shell Cu-$3d^{10}$ orbital in Cu_4H_3 [1], since our Bader charge calculation shows that the individual vertex Cu atoms lose only 0.32 electrons and the three face-center Cu atoms only lose 0.19 electrons per Cu. Therefore, we adopt a well-established empirical parameters: $U = 4.0$ eV [2] and investigate their impact on Cu_4H_3.

After structural optimization, the crystal structure with a Hubbard $U = 4.0$ eV correction exhibits negligible differences compared to the structure without correction, with the lattice constant expanding by approximately 0.42%, while the atomic positions remain unchanged during the optimization.

The impact of on-site Coulomb interactions on the electronic properties including band structure and electronic density of states (DOS) of Cu_4H_3 is shown in Figs. S1(a)-S1(c). It turns out that the impact of on-site Coulomb interactions on electronic properties is primarily concentrated in the Cu-3d orbitals, which causes the dominant energy distribution of the Cu-3d orbitals to shift from the range of -6 to 1 eV down to -7 to -2 eV, as shown in the zoomed-in electronic DOS of Fig. S1(c). The trend is consistent with that observed in CuTe, where the Cu bands, originally ranging from -2 to -4 eV, shift to -4 to -6 eV when considering PBE+U [3]. The on-site Coulomb interactions have negligible impact on the Cu-4s and H-1s orbitals near the E_F. As for the Cu-3d orbitals at E_F, their percentage decreases from 45.22% to 29.17% when the Hubbard $U = 4.0$ eV correction is applied. In turn, the percentage of Cu-4s and H-1s orbitals at E_F increase from 26.03% and 28.74% with $U = 0$ to 36.38% and 34.45% with $U = 4.0$ eV, respectively. In fact, the decrease in the relative percentage of Cu-3d orbital electrons at E_F along with the increased proportion of H-1s and Cu-4s orbital electrons at E_F is beneficial for superconductivity [4], as discussed in detail in Sec. IV A and IV B.

At last, we investigate the influence of the electronic correlation effect on phonon spectra of Cu_4H_3, as shown in Fig. S1(d). When taking the Hubbard $U = 4.0$ eV into consideration for Cu-3d orbitals, the main feature is that more phonon softening points occur, specifically points X and M. Since the subsequent self-consistent harmonic approximation (SSCHA) calculation demonstrates that the imaginary frequency of point M can be suppressed by finite temperature, the structure stability will not be affected by the correlation effect of Cu-3d orbitals. The trend is also similar to CuTe, where it is the strong correlation effect of electrons that leads to phonon softening or the imaginary frequency [3]. For Cu_4H_3, the softening of phonon is generally accompanied by an increase in the EPC constant λ (see Sec. IV C for details), which might be beneficial for superconductivity to some extent.

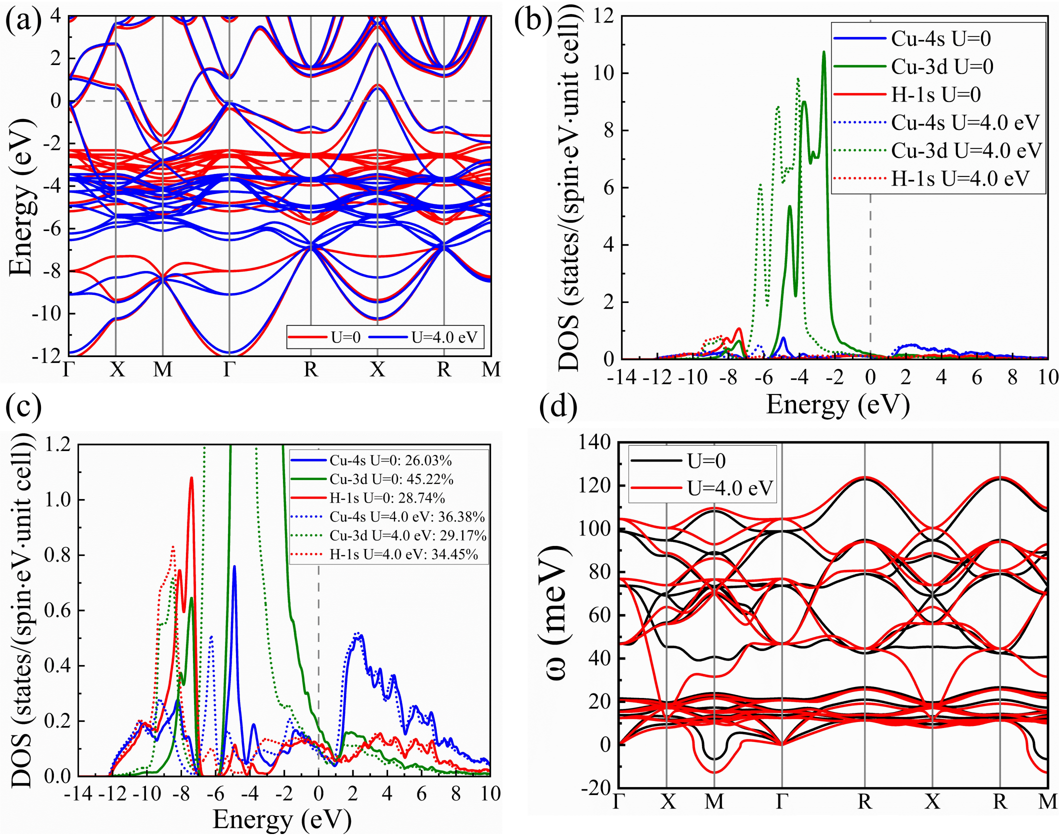

FIG. S1. (a) Calculated bulk band structures, (b) global, (c) zoomed-in electronic DOS, and (d) phonon spectra of cubic Cu_4H_3 using GGA ($U = 0$) and GGA+$U = 4.0$ eV methods. The band structures calculated by GGA and GGA+$U = 4.0$ eV are denoted by red and blue lines, respectively. The electronic DOS of Cu-4s, Cu-3d and H-1s orbitals are colored blue, green and red in panels (b) and (c). The DOS calculated using GGA and GGA+$U = 4.0$ eV are represented by solid and dotted lines, respectively in panels (b) and (c). The percentage DOS of Cu-4s, Cu-3d and H-1s orbitals at E_F are marked in panel (c). The phonon spectra calculated by GGA and GGA+$U = 4.0$ eV methods are denoted by black and red lines, respectively.

B. Band Structures

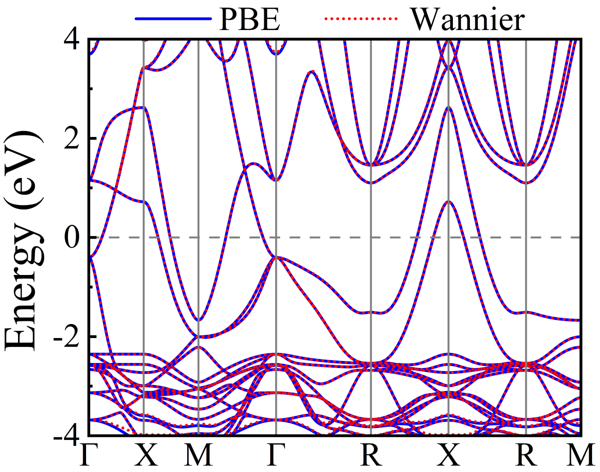

FIG. S2. Calculated bulk band structures of cubic Cu_4H_3, where the blue lines are calculated using the first-principles PBE functional, and the red dotted lines are simulated using the Wannier interpolation technology, respectively.

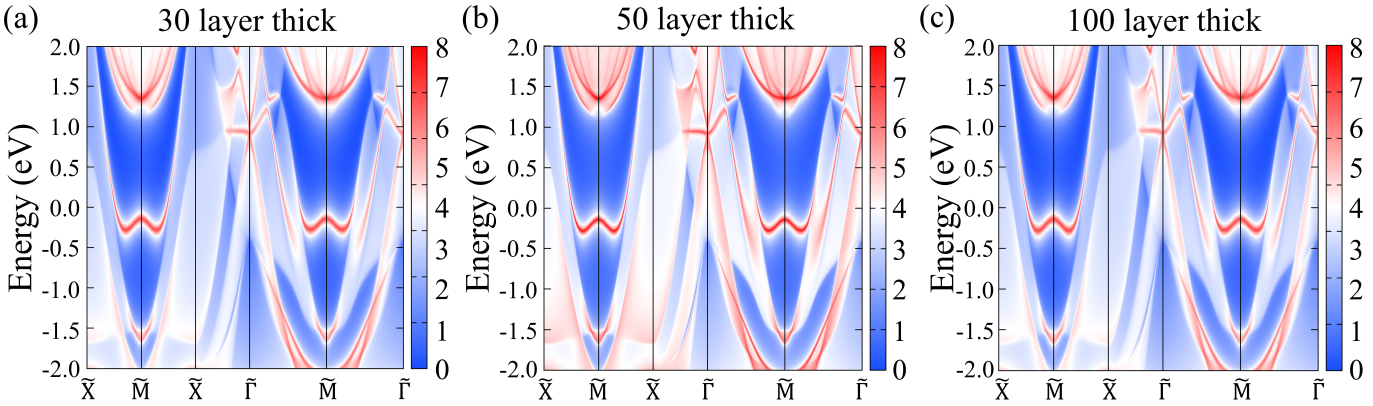

FIG. S3. Calculated surface states of Cu_4H_3 using (a) 30-layer (210 atoms), (b) 50-layer (350 atoms), and (c) 100-layers (700 atoms) thick slabs on the (001) surface, with a vacuum thickness set to 20 Å.

C. SSCHA Calculations

During the SSCHA minimization procedure, H atoms consistently occupied the octahedral (O_h) interstitial sites in face-centered-cubic (fcc) Cu. In this way, an additional SSCHA quantum pressure [5]

$$p_q = -\frac{1}{\Omega}\frac{\partial \mathcal{F}}{\partial \epsilon}\bigg|_{\epsilon=0} \tag{S1}$$

can be evaluated using the volume of the cell Ω, the SSCHA free energy $\mathcal{F}$ and the strain ϵ of the harmonic lattice constant.

The key of combining SSCHA phonons with the electron-phonon matrix elements to calculate superconducting T_c lies in: using the harmonic electron-phonon coupling (EPC) matrix elements, SSCHA phonon frequencies $\omega_{\mathbf{q}\nu}$ and polarization vectors $\hat{e}_{\mathbf{q}\nu}$ obtained by diagonalizing the Fourier interpolated SSCHA force constants to evaluate the Eliashberg spectral function [6]

$$\alpha^2 F(\omega) = \frac{1}{2\pi N(E_F) N_{\mathbf{q}}} \sum_{\mathbf{q}\nu} \delta(\omega - \omega_{\mathbf{q}\nu}) \frac{\gamma_{\mathbf{q}\nu}}{\hbar\omega_{\mathbf{q}\nu}}, \tag{S2}$$

where $\gamma_{\mathbf{q}\nu}$ denotes the phonon linewidth

$$\gamma_{\mathbf{q}\nu} = \frac{2\pi\omega_{\mathbf{q}\nu}}{N_{\mathbf{k}}} \sum_{\mathbf{k}mn} \left|g^{mn}_{\mathbf{k},\mathbf{q}\nu}\right|^2 \times \delta(E_{\mathbf{k}+\mathbf{q},m} - E_F)\delta(E_{\mathbf{k},n} - E_F), \tag{S3}$$

$N_{\mathbf{k}}$ and $N_{\mathbf{q}}$ denote the number of electron and phonon momentum points in Brillouin zone sampling. The double delta function is

$$\xi(\mathbf{q}) = \frac{1}{N_{\mathbf{k}}} \sum_{\mathbf{k}mn} \delta(E_{\mathbf{k}+\mathbf{q},m} - E_F)\delta(E_{\mathbf{k},n} - E_F). \tag{S4}$$

The EPC matrix element is

$$g^{mn}_{\mathbf{k},\mathbf{q}\nu} = (\frac{\hbar}{2M\omega_{\mathbf{q}\nu}})^{1/2} \left| \langle\psi_{m,\mathbf{k}+\mathbf{q}}| \frac{dV_{\mathrm{SCF}}}{d\hat{u}_{\mathbf{q}\nu}} \cdot \hat{e}_{\mathbf{q}\nu} |\psi_{n,\mathbf{k}}\rangle \right|, \tag{S5}$$

where $\psi_{n,\mathbf{k}}$ and $\psi_{m,\mathbf{k}+\mathbf{q}}$ denote electronic wavefunction with band index m, n and wavevector $\mathbf{k}$ and $\mathbf{k}+\mathbf{q}$. M denotes the atomic mass and ν is phonon index. $\omega_{\mathbf{q}\nu}$ and $\hat{e}_{\mathbf{q}\nu}$ represent the vibrational frequency and the polarization vector of the ν-th phonon mode at wavevector $\mathbf{q}$, respectively. The $\frac{dV_{\mathrm{SCF}}}{d\hat{u}_{\mathbf{q}\nu}}$ term describes the variation of the self-consistent potential caused by atomic vibrations. In this way, spectral function can be expressed as

$$\alpha^2F(\omega) = \frac{1}{N_{\mathbf{q}}} \sum_{\mathbf{q}\nu mn} \frac{\hat{e}^m_{\mathbf{q}\nu}\Delta^{mn}_{\mathbf{q}}\hat{e}^{n*}_{\mathbf{q}\nu}}{2\sqrt{M_m}\sqrt{M_n}\omega_{\mathbf{q}\nu}} \delta(\omega - \omega_{\mathbf{q}\nu}). \tag{S6}$$

The harmonic matrix element $\Delta^{mn}_{\mathbf{q}}$ is defines as

$$\begin{aligned}\Delta^{mn}_{\mathbf{q}} = \frac{1}{N(E_F)N_{\mathbf{k}}} \sum_{\mathbf{k}m'n'} &\langle\psi_{m',\mathbf{k}+\mathbf{q}}| \frac{dV_{\mathrm{SCF}}}{d\hat{u}^{m'}_{\mathbf{q}\nu}} |\psi_{n',\mathbf{k}}\rangle \langle\psi_{n',\mathbf{k}}| \frac{dV_{\mathrm{SCF}}}{d\hat{u}^{n'}_{\mathbf{q}\nu}} |\psi_{m',\mathbf{k}+\mathbf{q}}\rangle \\ &\times \delta(E_{\mathbf{k}+\mathbf{q},m'} - E_F)\delta(E_{\mathbf{k},n'} - E_F).\end{aligned} \tag{S7}$$

In this way, once the harmonic $\Delta^{mn}_{\mathbf{q}}$, SSCHA phonon frequencies $\omega_{\mathbf{q}\nu}$ and SSCHA polarization vectors $\hat{e}_{\mathbf{q}\nu}$ are obtained, the spectral function $\alpha^2F(\omega)$ can be determined. The EPC constant and logarithmic average frequency can be represented as

$$\lambda = 2\int \frac{\mathrm{d}\omega}{\omega}\alpha^2F(\omega), \tag{S8}$$

$$\omega_{\log} = \exp\left[\frac{2}{\lambda}\int \frac{\mathrm{d}\omega}{\omega}\alpha^2F(\omega)\log(\omega)\right], \tag{S9}$$

respectively. The anharmonic McMillan-Allen-Dynes T_c can thus be obtained using

$$T_c = \frac{\hbar\omega_{\log}}{1.2k_B}\exp\left[\frac{-1.04(1+\lambda)}{\lambda - \mu^*(1+0.62\lambda)}\right]. \tag{S10}$$

.

D. Electron-Phonon Coupling and Superconductivity

The fully anisotropic Migdal-Eliashberg (M-E) equations [7–9] can be describes as follows,

$$\begin{aligned}Z(\mathbf{k}, i\omega_n) = 1 + \frac{\pi T}{N(E_{\mathrm{F}})\omega_n} &\sum_{\mathbf{k}'n'} \frac{\omega_{n'}}{\sqrt{\omega^2_{n'} + \Delta^2(\mathbf{k}', i\omega_{n'})}} \\ &\times \delta(E_{\mathbf{k}'} - E_F)\lambda(\mathbf{k}, \mathbf{k}', n - n'),\end{aligned} \tag{S11}$$

$$\begin{aligned}Z(\mathbf{k}, i\omega_n)\Delta(\mathbf{k}, i\omega_n) = \frac{\pi T}{N(E_{\mathrm{F}})} &\sum_{\mathbf{k}'n'} \frac{\Delta(\mathbf{k}', i\omega_{n'})}{\sqrt{\omega^2_{n'} + \Delta^2(\mathbf{k}', i\omega_{n'})}} \\ &\times \delta(E_{\mathbf{k}'} - E_F)\left[\lambda(\mathbf{k}, \mathbf{k}', n - n') - \mu^*\right],\end{aligned} \tag{S12}$$

where $Z(\mathbf{k}, i\omega_n)$ and $\Delta(\mathbf{k}, i\omega_n)$ are the mass renormalization function and superconducting gap function, respectively. The $\mathbf{k}$, n and μ^* denote the electronic wave vector, band index, and the Morel-Anderson semiempirical Coulomb repulsion pseudopotential [10], respectively. The anisotropic EPC strength $\lambda(\mathbf{k}, \mathbf{k}^{'}, n - n^{'})$ can be written as,

$$\lambda\left(\mathbf{k}, \mathbf{k}', n - n'\right) = N(E_{\mathrm{F}}) \sum_{\mathbf{q}\nu} \frac{2\omega_{\mathbf{q}\nu}}{\left(\omega_n - \omega_{n'}\right)^2 + \omega_{\mathbf{q}\nu}^2} \left|g_{\mathbf{k}\mathbf{k}'}^{\nu}\right|^2, \tag{S13}$$

where $N(E_{\mathrm{F}})$, $\mathbf{q}$ and ν represent the electronic density of states (DOS) at the Fermi energy, the wave vector, and the branch of phonon, respectively. Further, ω_n represents the Matsubara frequencies, which is represented as $\omega_n = (2n + 1)\pi T$, and $g_{\mathbf{k}\mathbf{k}'}^{\nu}$ represents the EPC matrix element. Using these parameters, the coupled M-E equations (Eqs. (S11) and (S12)) can be solved self-consistently along the imaginary axis at Matsubara frequencies ω_n for each temperature T.

Calculations of the specific heat difference, as well as the entropy difference were as follows,

$$\Delta C(T) = -T \frac{\partial^2 \Delta F}{\partial T^2}\bigg|_V, \tag{S14}$$

$$\Delta S(T) = -\frac{\partial \Delta F}{\partial T}\bigg|_V = -\int \frac{\Delta C(T)}{T} dT. \tag{S15}$$

Here, ΔF denotes the free energy difference between the superconducting and normal states and can be written as follows [11, 12],

$$\begin{aligned}\Delta F = -\pi T \sum_{n\mathbf{k}j} & \left[\sqrt{\omega_j^2 + \Delta_{n\mathbf{k}}^2\left(i\omega_j\right)} - \left|\omega_j\right|\right] \times \delta\left(E_{n\mathbf{k}} - E_F\right) \\ & \times \left[Z_{n\mathbf{k}}\left(i\omega_j\right) - Z_{n\mathbf{k}}^N\left(i\omega_j\right) \frac{\left|\omega_j\right|}{\sqrt{\omega_j^2 + \Delta_{n\mathbf{k}}^2\left(i\omega_j\right)}}\right],\end{aligned} \tag{S16}$$

where Z^N represents the mass renormalization function of the normal state N, calculated by setting $\Delta\left(\mathbf{k}, i\omega_n\right) = 0$ in Eq. (S11).

II. SYNTHESIS STRATEGIES

A. The Nudged Elastic Band (NEB) Simulations and Kinetic Stability

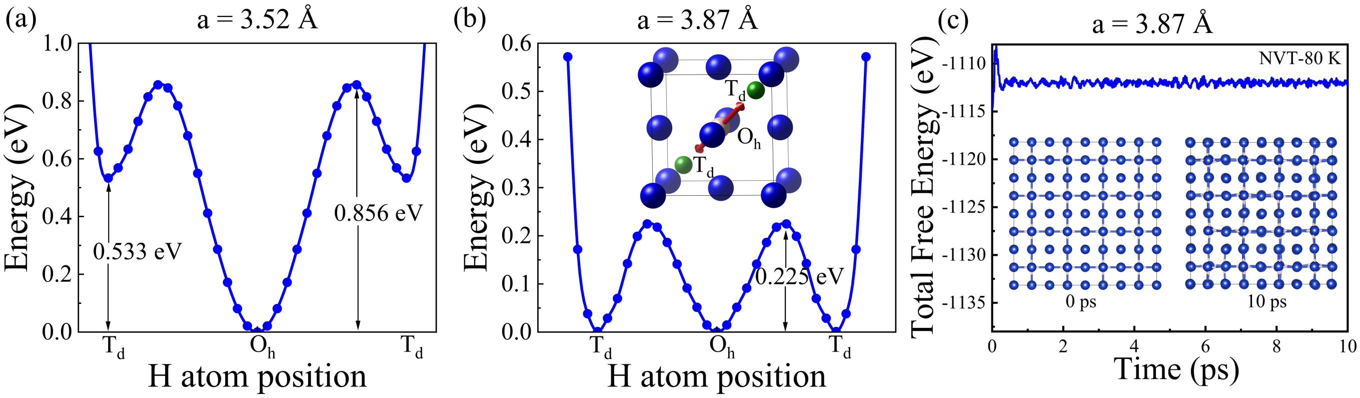

FIG. S4. The nudged elastic band (NEB) simulations and kinetic stability. The calculated total energy, accounting for quantum zero-point energy (ZPE), for a single H atom in fcc Cu with a lattice constant of (a) 3.52 Å (60 GPa) and (b) 3.87 Å in a conventional cell, along the [111] diagonal direction T_d-O_h-T_d. The inset of (b) shows the octahedral interstitial site O_h (gray pink ball) and tetrahedral interstitial site T_d (green ball). (c) The total free energy as a function of *ab initio* molecular dynamics (AIMD) simulation time for a $4 \times 4 \times 4$ supercell containing a single H atom in fcc Cu, with a lattice constant of 3.87 Å at 80 K in an NVT ensemble. The insets display corresponding structure snapshots at 0 and 10 ps, respectively.

Two competitive interstitial positions of hydrogen in fcc copper are the O_h and tetrahedral (T_d) interstitial sites [13], as shown in the inset of Fig. S4(b). Here, we take the quantum zero-point energy (ZPE) into consideration and compare the total energy of the two interstitial sites for different lattice constant of Cu, as displayed in Figs. S4(a) and S4(b). It turns out that as the lattice constant of Cu changes from 3.52 to 3.87 Å, the O_h interstitial site consistently remains the most stable position for H, with an energy advantage of 0.533 eV per unit lower than that of the T_d site at a lattice constant of 3.52Å. At 3.87 Å, the energy of the two sites becomes comparable. This suggests that when the lattice constant is less than 3.87 Å and Cu retains its fcc framework, the O_h interstitial sites are more stable for H atoms. This is consistent with experimental reports [13]. Furthermore, the energy barrier from the O_h to T_d site varies from 0.856 eV/unit at a lattice constant of 3.52 Å to 0.225 eV/unit at a lattice constant of 3.87 Å, indicating the local stability of H against thermal fluctuations.

The results of the NEB simulations above are consistent with the kinetic *ab initio* molecular dynamics (AIMD) simulations of H in different lattice constants of fcc Cu, as displayed in Figs. 1(d) and S4(c). Here, the lattice constant of the focused cubic Cu_4H_3 is 3.83 Å at ambient pressure, indicating that during the kinetic depressurization process from 60 GPa to 1 atm, H is expected to consistently occupy the O_h interstitial sites, as tested in Fig. 1(d).

B. Comparison with Experimental Data

A comparison of the volume-pressure (V-P) curves and points of copper hydrides, derived from experimental data, with our theoretical calculations is displayed in Fig. 1(a). (1) First, the V-P curve we calculated for cubic-CuH with known rock-salt structure (solid purple line) closely matches the equations-of-stat (EOS) curve for fcc-CuH from Ref. [14](dotted cyan line). This serves as a benchmark for further analysis of the unclear hydrogen concentration in cubic CuH_x, as displayed in Fig. 1(a). (2) The diffraction data (open light green squares) for fcc CuH_x [14] fall between the curves for cubic-Cu_4H_3 (solid blue line) and cubic-CuH (solid purple line) calculated in this work, as displayed in Fig. 1(a). This suggests that various concentrations of CuH_x, from $CuH_{0.75}$ to CuH, can be synthesized under different pressure and temperature. (3) The diffraction data (open red triangles) and EOS (dashed red line) for fcc-CuH_x, with so-called $x \sim 0.65$ reported in Ref. [15], seem to align with our calculated V-P curve of cubic-Cu_4H_3 (solid blue line), as shown in Fig. 1(a). To clarify this discrepancy and figure out the actual hydrogen concentration in CuH_x with unknown structure, we use the data derived from fcc Cu and cubic Cu_4H_3 with known structures calculated at 1 atm in this work, and perform a linear fit to establish the relationship between volume (V) and hydrogen concentration (n), given by $V = 2.70\,n + 12.00$, as displayed in Fig. S5. Here, the slope of 2.70 Å^3 per H denotes that each additional H atom makes the volume expand by 2.70 Å^3, which is smaller than the slope of 2.90 Å^3 per H used in Ref. [15]. The

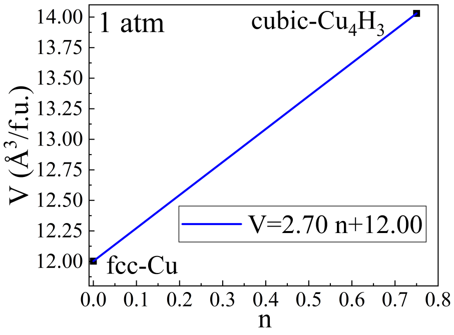

FIG. S5. Variation of volume with H concentration. The solid black squares denote the calculated results for fcc-Cu and cubic-Cu_4H_3 at 1 atm. Solid blue line is the linear fitting for the points, $V = 2.70\,n + 12.00$, where V denotes volume per formula unit of Cu and n denotes H concentration.

underestimation of the H concentration in fcc-CuH_x as 0.65 [15] arose from using the average slope of the volume (V)-H concentration relationship (n) curve for d-metal hydrides [16], rather than that of the actual copper hydrides. In fact, the focused cubic-$CuH_{0.75}$ phase may have been synthesized by two independent groups: one at 30-50 GPa and 1000-3000 K (open red triangles) [15], and the other synthesized at pressures exceeding 60 GPa and temperatures above 2000 K, which was then quenched to 300 K at fixed pressure (open light green squares) [14].

C. Kinetic Simulations of Cubic CuH

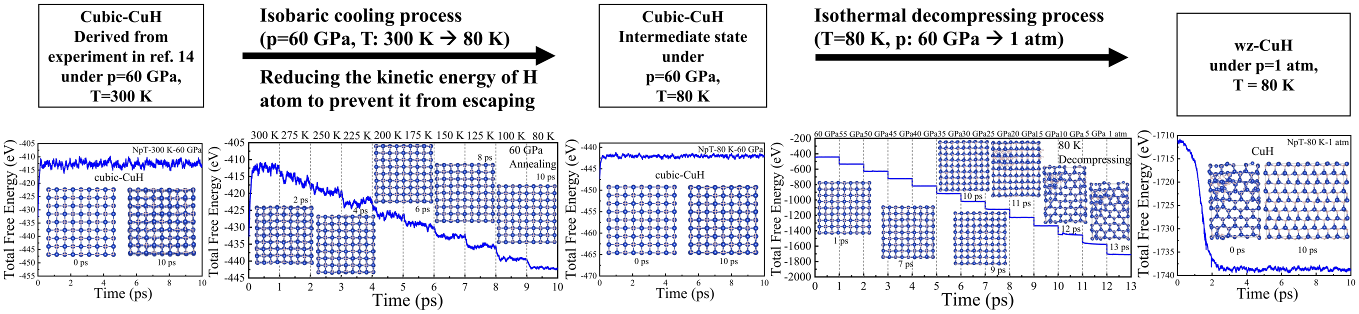

FIG. S6. Flowchart of the experimental synthesis routes and simulations of the kinetic processes for cubic CuH. The starting point is the experimentally synthesized cubic CuH at around 60 GPa and room temperature [14], as displayed in Fig. 1(a). The AIMD simulation of the kinetic stability of cubic-CuH with NpT ensemble at 60 GPa and 300 K is displayed below. The insets display the snapshots of the trajectories of cubic-CuH at 0 (left) and 10 ps (right), respectively. Next, an isobaric cooling process with pressure fixed at 60 GPa while temperature varying from 300 to 80 K is designed to reduce the kinetic energy of H atoms to prevent them from escaping during the subsequent decompressing process. Note that the annealing process lasts for 10 ps, with a temperature interval of 25 K and time interval of 1 ps. Each cooling step is also conducted with NpT ensemble and screenshot of structures at 2, 4, 6, 8 and 10 ps are displayed in the insets. Then, kinetic stability of cubic-CuH is tested with NpT ensemble at 80 K with pressure of around 60 GPa, lasting for 10 ps. The insets display the snapshots of the trajectories of cubic-CuH at 0 (left) and 10 ps (right), respectively. Furthermore, kinetic process of decompressing at 80 K is simulated, with pressure varying from 60 GPa to atmospheric pressure. The pressure is reduced by 5 GPa per step (1 ps) lasting for 13 ps. The insets display the snapshots of cubic CuH at 1, 7, 9, 10, 11, 12 and 13 ps. It turns out that cubic-CuH can stay stable at 80 K when the pressure exceeds 20 GPa (9 ps). However, when further decreasing pressure to 15 GPa at 10 ps, the lattice displays distortion, with hydrogen atoms showing a trend to escape from the O_h interstitial sites of fcc-Cu. Moreover, at 10 GPa (11 ps), phase segregation between H and Cu occurs, with H atoms accumulating in the top left corner of the inset at 11 ps. When further decreasing the pressure below 10 GPa, the lattice gradually transforms into hexagonal wurtizite-CuH (wz-CuH). Finally, at 80 K and ambient pressure, the AIMD simulation indicates that cubic-CuH phase completely transforms into wz-CuH and can remain stable.

III. STRUCTURE

A. Simulated X-Ray Diffraction and Neutron Diffraction Pattern

Neutron diffraction (ND) plays an important role in characterizing H atoms in metal hydrides. Figure S7 displays the ND and x-ray diffraction (XRD) pattern for fcc Cu and cubic Cu_4H_3. The patterns of ND and XRD for fcc-Cu in Figs. S7(a) and S7(b) display negligible difference. For cubic Cu_4H_3 displayed in Figs. S7(c) and S7(d), the signals of hydrogen are clearly characterized by ND, while the signals of copper are more easily characterized by XRD.

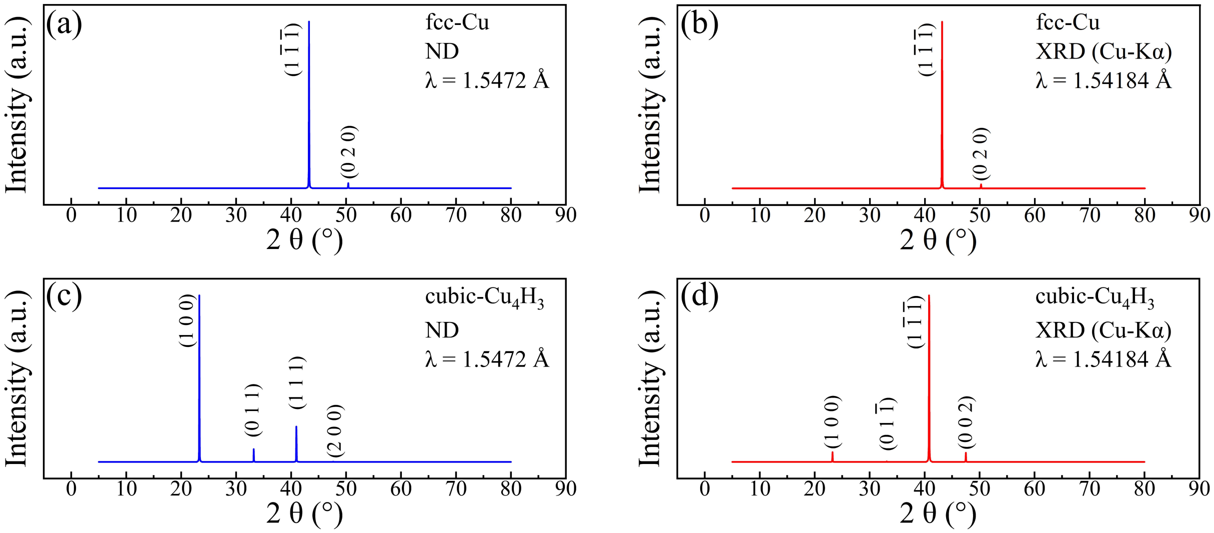

FIG. S7. Simulated neutron diffraction (ND) and x-ray diffraction (XRD) pattern for (a)-(b) fcc Cu and (c)-(d) cubic Cu_4H_3.

IV. ELECTRON-PHONON COUPLING AND SUPERCONDUCTIVITY

A. Gaspari-Gyorffy Theory

In McMillan's strong coupling superconductor theory [17], the EPC constant is given by,

$$\lambda = \frac{N(E_F)\langle I^2\rangle}{M\langle\omega^2\rangle}, \tag{S17}$$

where M, $N(E_F)$ and $\langle I^2\rangle$ denote the atomic mass, the DOS at Fermi level and the square of the EPC matrix element averaged over the Fermi surface, respectively; $\langle\omega^2\rangle$ is an average of the square of the phonon frequency,

$$\langle\omega^2\rangle = \frac{\int \mathrm{d}\omega\omega\alpha^2F(\omega)}{\int \mathrm{d}\omega/\omega\alpha^2F(\omega)}. \tag{S18}$$

For a metal-hydrogen system with a large mass difference and perfect separation of vibration modes between metal and hydrogen, the EPC constant λ can be further divided into two parts,

$$\lambda = \lambda_{\mathrm{Metal}} + \lambda_{\mathrm{H}} = \frac{\eta_{\mathrm{Metal}}}{M_{\mathrm{Metal}}\langle\omega^2\rangle_{\mathrm{Metal}}} + \frac{\eta_{\mathrm{H}}}{M_{\mathrm{H}}\langle\omega^2\rangle_{\mathrm{H}}}, \tag{S19}$$

where the Hopfield parameter [18] η is given by

$$\eta = N(E_F)\langle I^2\rangle. \tag{S20}$$

To further estimate the Hopfield parameter and derive the EPC constant λ, Gaspari, Gyorffy and Hopfield all take the assumption that the local effects, like the extra scattering due to the displacement of an ion, are dominated by the local potential [18, 19]. By further assume the potential is spherically symmetric, the Bloch function can be expanded in the angular-momentum representation,

$$\psi_{\mathbf{k}}(\mathbf{r}) = \sum_{l} \sum_{m=-l}^{l} a_{lm}(\mathbf{k}) R_l(r, E_{\mathbf{k}}) Y_l^m(\theta, \phi), \tag{S21}$$

where the coefficient $a_{lm}(\mathbf{k})$ is determined by the scattering properties of the crystal structure, $R_l(r, E_{\mathbf{k}})$ is the scattering solution of the radial Schrödinger equation which includes the ion effect, $E_{\mathbf{k}}$ is the eigenvalue of one-electron Bloch funciton $\psi_{\mathbf{k}}(\mathbf{r})$, and $Y_l^m(\theta, \phi)$ denotes the spherical harmonic function [19]. Finally, the central result of the Gaspari-Gyorffy theory [19] is,

$$\eta = N(E_F)\langle I^2 \rangle = \frac{2ME_F}{\hbar^2 \pi^2} \frac{1}{N(E_F)} \sum_{l} \frac{2(l+1)\sin^2(\delta_{l+1} - \delta_l) N_l(E_F) N_{l+1}(E_F)}{N_l^{(1)} N_{l+1}^{(1)}}, \tag{S22}$$

where $N_l(E_F)$ and $N_l^{(1)}$ denote the lth partial DOS and the free-scatter DOS, respectively; δ_l is the phase shift of angular character l of the potential.

Using the rigid-ion approximation, it is found that in transition metal hydride system, the potential of H is characterized by large s-wave phase shifts, with the phase shift δ_0 of H close to a resonance, $\delta_0 \sim \pi/2$. Therefore, the Hopfield constant of H, η_{H}, is expected to be dominated by an s-p scattering mechanism. The variation of η_{H} will be determined by the magnitude at the H site and the partial DOS of s and p states at E_F, relative to the total DOS, as reported in Ref. [20]. This is the reason why we emphasize the importance of H-1s and Cu-4s orbital electrons at E_F in facilitating a large EPC in $\mathrm{Cu_4H_3}$. In the next subsection, we further demonstrate that H-1s and Cu-4s orbital electrons in cubic $\mathrm{Cu_4H_3}$ are more likely to couple with the vibration of H by examining the band structures modified by H vibration.

B. Band Structures Modified by H Vibration

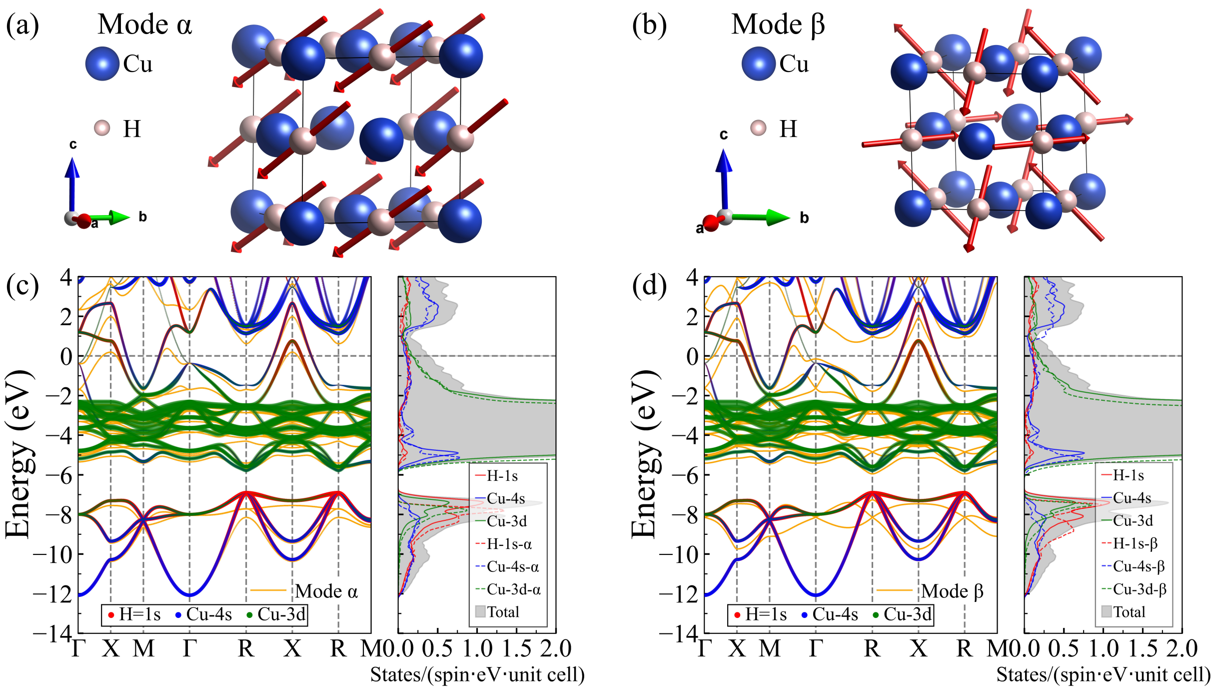

FIG. S8. The vibrational visualization images of (a) mode α (the 13th mode) and (b) mode β (the 16th mode) in Fig. 4(a) are shown, with arrows indicating the vibrational directions of the H atoms. The modified band structures due to the vibration modes of H in (c) mode α and (d) mode β are presented, with the displacement of H in both cases set to 0.58 Å. In the orbital-projected band structure (left panel) and electronic DOS (right panel) of (c) and (d), the H-1s, Cu-4s and Cu-3d states are colored red, blue and green, respectively. The modified band structures due to the vibration of H are represented by orange lines. The electronic DOS of Cu_4H_3 in the equilibrium and modified atomic positions are shown by solid and dashed lines, respectively. The total DOS in the equilibrium atomic position of Cu_4H_3 is shaded grey.

To confirm that the H-1s and Cu-4s orbital electrons in cubic Cu_4H_3 are more likely to couple with the vibration of H, we illustrate this by considering two vibration modes of H (mode α and mode β in Fig. 4(a)) and investigating the band structures of Cu_4H_3 modified by H vibrations, as shown in Fig. S8. Mode α and mode β correspond to the 13th and 16th harmonic modes at Γ point of Fig. 4(a). In mode α, all the H atoms vibrate primarily along the [111] direction with the displacement of H to be 0.58 Å and negligible displacement of Cu atoms. In mode β, three H atoms vibrate along the $[0\bar{1}1]$, $[10\bar{1}]$, and $[\bar{1}10]$ directions, with the displacement of H to be 0.58 Å and negligible displacement of Cu atoms. In Figs. S8(c) and S8(d), it can be seen that for the points where the H-1s orbital dominates (especially in the energy ranges of -10 to -8 eV and -2 to 4 eV), the vibration of H causes noticeable changes in the electronic structure. Second to the the H-1s orbital, the Cu-4s orbital-dominated band structures also undergo significant modifications in the energy ranges of -6 to -4 eV and -2 to 4 eV following the displacement of H. With respect to the Cu-3d orbitals in the range of -6 to -2 eV, they are only weakly affected by the H vibration, manifesting the weak EPC between them. In short, the conclusion that the H-1s and Cu-4s orbital electrons in cubic Cu_4H_3 are more likely to couple with the vibration of H holds true in Cu_4H_3, which is also corroborated by the Gaspari-Gyorffy theory in subsequent subsection.

C. Discussion on Fermi Surface Nesting

The EPC constant λ can also be expressed as a sum of the EPC strength $\lambda_{\mathbf{q}\nu}$ over the wave vector $\mathbf{q}$ and the phonon branch ν

$$\lambda = \sum_{\mathbf{q}\nu} \lambda_{\mathbf{q}\nu}, \tag{S23}$$

where the EPC strength is

$$\lambda_{\mathbf{q}\nu} = \frac{\gamma_{\mathbf{q}\nu}}{\pi\hbar N(E_F)\omega_{\mathbf{q}\nu}^2}. \tag{S24}$$

By substituting the phonon linewidth $\gamma_{\mathbf{q}\nu}$ of Eq. (S3) into the EPC strength $\lambda_{\mathbf{q}\nu}$, we can derive,

$$\lambda_{\mathbf{q}\nu} = \frac{2}{\hbar\omega_{\mathbf{q}\nu} N_{\mathbf{k}} N(E_F)} \sum_{\mathbf{k}mn} |g_{\mathbf{k},\mathbf{q}\nu}^{mn}|^2 \times \delta(E_{\mathbf{k}+\mathbf{q},m} - E_F)\delta(E_{\mathbf{k},n} - E_F). \tag{S25}$$

Equation (S25) indicates that increasing the EPC matrix element $g_{\mathbf{k},\mathbf{q}\nu}^{mn}$ and the double delta function at Fermi level $\xi(\mathbf{q}) = \frac{1}{N_{\mathbf{k}}} \sum\limits_{\mathbf{k}mn} \delta(E_{\mathbf{k}+\mathbf{q},m} - E_F)\delta(E_{\mathbf{k},n} - E_F)$ will be beneficial to the EPC strength $\lambda_{\mathbf{q}\nu}$ or EPC constant λ, as well as superconducting T_c.

We further clarify the relationship between FSN and the double delta function in Eq. (1) of the manuscript. The generalized static electronic susceptibility $\chi_{\mathbf{q}}$ usually leads to the soft/imaginary phonon in charge-density-wave (CDW) materials according to

$$\omega_{\mathbf{q}}^2 = \Omega_{\mathbf{q}}^2 - 2\Omega_{\mathbf{q}}\chi_{\mathbf{q}}, \tag{S26}$$

where $\Omega_{\mathbf{q}}$ denotes the bare phonon frequency and $\omega_{\mathbf{q}}$ denotes the screened/softened phonon under random phase approximation [21]. The generalized static electronic susceptibility $\chi_{\mathbf{q}}$ also has contributions from FSN and EPC,

$$\chi_{\mathbf{q}} = \sum_{\mathbf{k}} |g_{\mathbf{k},\mathbf{k}+\mathbf{q}}|^2 \frac{f(\epsilon_{\mathbf{k}}) - f(\epsilon_{\mathbf{k}+\mathbf{q}})}{\epsilon_{\mathbf{k}+\mathbf{q}} - \epsilon_{\mathbf{k}}}, \tag{S27}$$

where the EPC matrix element $g_{\mathbf{k},\mathbf{k}+\mathbf{q}}$ couples electronic states $\mathbf{k}$ and $\mathbf{k}+\mathbf{q}$ with a phonon of momentum $\mathbf{q}$ and the static Linhard susceptibility of pure electronic contribution is given by,

$$\chi'_{\mathbf{q}} = \sum_{\mathbf{k}} \frac{f(\epsilon_{\mathbf{k}}) - f(\epsilon_{\mathbf{k}+\mathbf{q}})}{\epsilon_{\mathbf{k}+\mathbf{q}} - \epsilon_{\mathbf{k}}} \tag{S28}$$

($f(\epsilon)$ is the Fermi-Dirac function of the eigenvalue ϵ). On the one hand, it is the divergence of the real part of the susceptibility $\chi'_{\mathbf{q}}$ that induces phonon softening/CDW instability while $\chi'_{\mathbf{q}}$ is difficult to detect experimentally. On the other hand, the imaginary part of susceptibility $\chi''_{\mathbf{q}}$ reflects the Fermi surface topology and can be measured experimentally. Also, $\chi''(\mathbf{q}, \omega \to 0)$ is easier to be calculated as,

$$\lim_{\omega \to 0} \frac{\chi''(\mathbf{q}, \omega)}{\omega} = \sum_{\mathbf{k}} \delta(E_{\mathbf{k}+\mathbf{q},m} - E_F)\delta(E_{\mathbf{k},n} - E_F) \tag{S29}$$

Therefore, the double delta function is often presented in first-principles studies as a quantitative test of the FSN as reported in Ref [22, 23]. At last, we would like to mention that one of the similar origins of the CDW and high-T_c superconductivity is that they are generally induced by phonon softening to give rise to either the imaginary frequency or a large EPC constant λ according to Eq. (S26).

D. Impact of the Coulomb Repulsion on Superconducting Gap

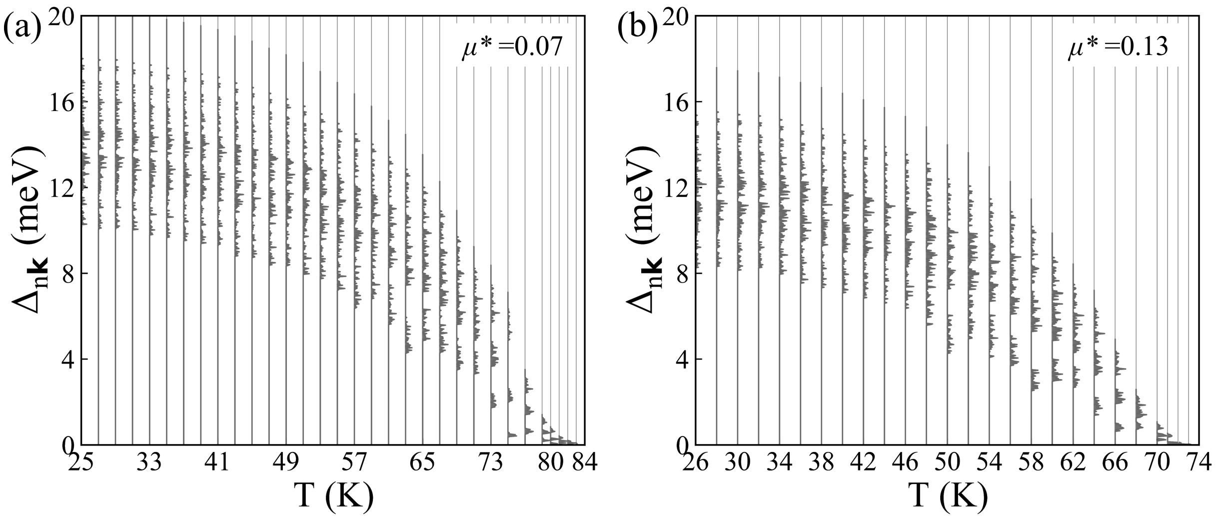

FIG. S9. Temperature dependent anisotropic superconducting gap $\Delta_{n\mathbf{k}}$ with the semiempirical Coulomb repulsion pseudopotential (a) $\mu^* = 0.07$ and (b) $\mu^* = 0.13$, respectively. The superconducting gap declines smoothly with the temperature and finally vanishes at around 83 and 73 K, respectively.

E. Impact of the External Strains on Phonon Spectra and Superconductivity

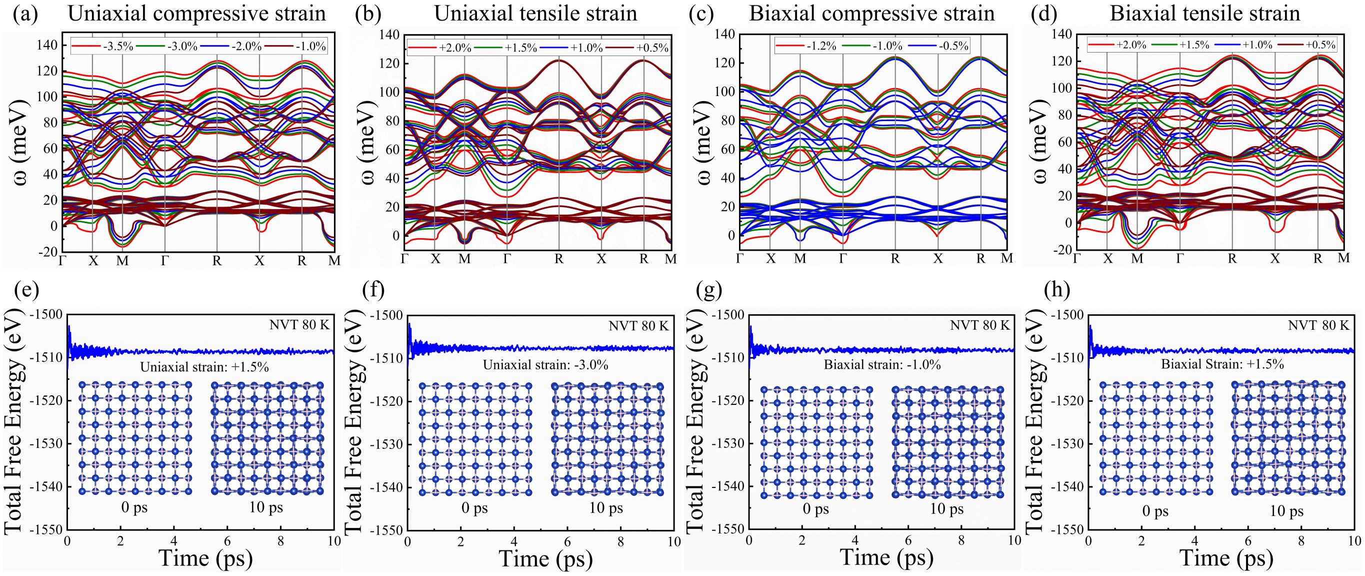

FIG. S10. Calculated phonon spectra of Cu_4H_3 under (a) uniaxial compressive and (b) uniaxial tensile strain along the z direction, as well as (c) biaxial compressive and (d) biaxial tensile strain along x and y directions. Specifically, the positive values indicate tensile strain and negative values indicate compressive strain. The total free energy as a function of AIMD simulation time for Cu_4H_3 is presented under (e) uniaxial compressive strain of 1.5%, (f) uniaxial tensile strain of 3.0%, (g) biaxial compressive strain of 1.0% and (h) biaxial tensile strain of 1.5% in an NVT ensemble, using a supercell size of $4 \times 4 \times 4$ unit cells. The insets of (e)-(g) exhibit snapshots of Cu_4H_3 at the corresponding moments.

We determine the stretching and compressive limits of Cu_4H_3 by gradually increasing external strain and calculating the corresponding phonon spectra. The results in Figs. S10(a)-S10(d) indicate that Cu_4H_3 can remain structurally

TABLE S1. Summary of the calculated McMillan-Allen-Dynes (M-A-D) superconducting T_c ($\mu^* = 0.1$), the EPC constant λ, and the logarithmic average frequency $\omega_{\log}$ of the free-state Cu_4H_3, as well as Cu_4H_3 under different uniaxial and biaxial strains.

system	M-A-D T_c (K)	λ	$\omega_{\log}$ (K)
free state	43.07	1.46	387.79
-3.0% uniaxial strain	36.27	1.48	322.66
+1.5% uniaxial strain	25.77	1.40	241.84
-1.0% biaxial strain	22.46	2.05	153.69
+1.5% biaxial strain	31.60	1.42	293.38

stable within the range of -3.0% to +1.5% for uniaxial strain and -1.0% to +1.5% for biaxial strain, where negative values denote compressive strain and positive values denote tensile strain. The structures at the stretching and compressive limits are also tested by AIMD simulations shown in Figs. S10(e)-S10(h).

We further evaluate the superconducting T_c of Cu_4H_3 at both extremes of external strain using the M-A-D formula, disregarding the imaginary frequency at point M, which has been shown to be suppressed by finite temperature in Fig. 4(a). The results reveal that compared to free-state Cu_4H_3, the superconducting T_c of Cu_4H_3 under strain decreases to some extent. Under external strain, when one direction contracts (or stretches), the other two directions will stretch (or contract) correspondingly. The contraction (or stretching) of the lattice constant typically leads to the hardening (or softening) of the phonon spectra, a decrease (or increase) in λ, and an increase (or decrease) in $\omega_{\log}$. On the one hand, the final T_c is the result of the competition between changes of λ and $\omega_{\log}$. On the other hand, it is worth noting that under external uniaxial or biaxial strain, the crystal symmetry is lowered compared to the cubic phase Cu_4H_3. While high-T_c usually favors for highly symmetric structures [24], this may also cause the decrease of T_c under external strain compared to the free-state Cu_4H_3. Despite this, when applying uniaxial strain of around 3%, the relatively high superconducting T_c of around 36.27 K can still be maintained, which decrease by 15.79% compared to the harmonic M-A-D T_c of the free-state Cu_4H_3. In this way, after solving the M-E equations, the liquid-nitrogen temperature region superconducting T_c (63-77 K) of Cu_4H_3 can still be expected under external strain.

[1] `https://pranabdas.github.io/espresso/hands-on/dft-u/`.

[2] L. Wang, T. Maxisch, and G. Ceder, Oxidation energies of transition metal oxides within the GGA + U framework, Phys. Rev. B **73**, 195107 (2006).

[3] S. Kim, B. Kim, and K. Kim, Role of coulomb correlations in the charge density wave of cute, Phys. Rev. B **100**, 054112 (2019).

[4] F. Belli, T. Novoa, J. Contreras-García, and I. Errea, *Strong correlation between electronic bonding network and critical temperature in hydrogen-based superconductors*, Nat. Commun. **12**, 5381 (2021).

[5] F. Belli and I. Errea, *Impact of ionic quantum fluctuations on the thermodynamic stability and superconductivity of* $\mathrm{LaBH_8}$, Phys. Rev. B **106**, 134509 (2022).

[6] The SSCHA website, `https://sscha.eu/Tutorials/tutorial_07_simple_electron_phonon/`.

[7] A. Migdal, *Interaction between electrons and lattice vibrations in a normal metal*, Sov. Phys. JETP **7**, 996 (1958).

[8] G. Eliashberg, *Interactions between electrons and lattice vibrations in a superconductor*, Sov. Phys. JETP **11**, 696 (1960).

[9] E. R. Margine and F. Giustino, *Anisotropic Migdal-Eliashberg theory using Wannier functions*, Phys. Rev. B **87**, 024505 (2013).

[10] P. Morel and P. W. Anderson, *Calculation of the Superconducting State Parameters with Retarded Electron-Phonon Interaction*, Phys. Rev. **125**, 1263 (1962).

[11] J. Bardeen and M. Stephen, *Free-Energy Difference Between Normal and Superconducting States*, Phys. Rev. **136**, A1485 (1964).

[12] H. J. Choi, M. L. Cohen, and S. G. Louie, *Anisotropic Eliashberg theory of* $\mathrm{MgB_2}$*:* T_c*, isotope effects, superconducting energy gaps, quasiparticles, and specific heat*, Physica C **385**, 66 (2003).

[13] J. Bugeat and E. Ligeon, *Lattice location and trapping of hydrogen implanted in FCC metals*, Phys. Lett. A **71**, 93 (1979).

[14] T. Meier, F. Trybel, G. Criniti, D. Laniel, S. Khandarkhaeva, E. Koemets, T. Fedotenko, K. Glazyrin, M. Hanfland, M. Bykov, G. Steinle-Neumann, N. Dubrovinskaia, and L. Dubrovinsky, Proton mobility in metallic copper hydride from high-pressure nuclear magnetic resonance, Phys. Rev. B **102**, 165109 (2020).

[15] J. Binns, M. Peña-Alvarez, M.-E. Donnelly, E. Gregoryanz, R. T. Howie, and P. Dalladay-Simpson, Structural studies on the cu–h system under compression, Engineering **5**, 505 (2019).

[16] B. Baranowski, S. Majchrzak, and T. B. Flanagan, *The volume increase of fcc metals and alloys due to interstitial hydrogen over a wide range of hydrogen contents*, J. Phys. F: Met. Phys. **1**, 258 (1971).

[17] W. L. McMillan, *Transition Temperature of Strong-Coupled Superconductors*, Phys. Rev. **167**, 331 (1968).

[18] J. J. Hopfield, Angular momentum and transition-metal superconductivity, Phys. Rev. **186**, 443 (1969).

[19] G. D. Gaspari and B. L. Gyorffy, *Electron-Phonon Interactions, d Resonances, and Superconductivity in Transition Metals*, Phys. Rev. Lett. **28**, 801 (1972).

[20] B. Stritzker, *Superconductivity in Metal-Hydrogen Systems* (Springer US, Boston, MA, 1983) pp. 309–320.

[21] Z. Wang, C. Chen, J. Mo, J. Zhou, K. P. Loh, and Y. P. Feng, Decisive role of electron-phonon coupling for phonon and electron instabilities in transition metal dichalcogenides, Phys. Rev. Res. **5**, 013218 (2023).

[22] M. D. Johannes and I. I. Mazin, *Fermi surface nesting and the origin of charge density waves in metals*, Phys. Rev. B **77**, 165135 (2008).

[23] W. E. Pickett and P. B. Allen, Superconductivity and phonon softening. iii. relation between electron bands and phonons in nb, mo, and their alloys, Phys. Rev. B **16**, 3127 (1977).

[24] M. R. Norman, *Materials design for new superconductors*, Rep. Prog. Phys. **79**, 074502 (2016).